Atomic Force Microscopy Stiffness Mapping in Human Aortic Smooth Muscle Cells

Claudie Petit, Ali-Akbar Karkhaneh Yousefi, Marine Guilbot, Vincent Barnier, Stéphane Avril, Nathalie Douard

Claudie Petit
Mines Saint-Etienne,
Université de Lyon, INSERM,
U 1059 SAINBIOSE,
Saint-Etienne F - 42023, France

Ali-Akbar Karkhaneh Yousefi
Mines Saint-Etienne,
Université de Lyon, INSERM,
U 1059 SAINBIOSE,
Saint-Etienne F - 42023, France

Marine Guilbot
Mines Saint-Etienne,
Université de Lyon, INSERM,
U 1059 SAINBIOSE,
Saint-Etienne F - 42023, France

Vincent Barnier
Mines Saint-Etienne,
Université de Lyon,
CNRS, UMR 5307 LGF,
Saint-Etienne F - 42023, France

Stéphane Avril[1]
Mines Saint-Etienne,
Université de Lyon, INSERM,
U 1059 SAINBIOSE,
Saint-Etienne F - 42023, France
e-mail: avril@emse.fr.

Atomic Force Microscopy Stiffness Mapping in Human Aortic Smooth Muscle Cells

Aortic smooth muscle cells (SMCs) play a vital role in maintaining mechanical homeostasis in the aorta. We recently found that SMCs of aneurysmal aortas apply larger traction forces than SMCs of healthy aortas. This result was explained by the significant increase of hypertrophic SMCs abundance in aneurysms. In this study, we investigate whether the cytoskeleton stiffness of SMCs may also be altered in aneurysmal aortas. For that, we use atomic force microscopy (AFM) nano-indentation with a specific mode that allows subcellular-resolution mapping of the local stiffness across a specified region of interest of the cell. Aortic SMCs from a commercial human lineage (AoSMCs, Lonza) and primary aneurysmal SMCs (AnevSMCs) are cultured in conditions promoting the development of their contractile apparatus, and seeded on hydrogels with stiffness properties of 12 kPa and 25 kPa. Results show that all SMCs exhibit globally a lognormal stiffness distribution, with medians in the range 10–30 kPa. The mean of stiffness distributions is 16 kPa in aneurysmal SMCs and 12 kPa in healthy cells, but the differences are not statistically significant due to the large dispersion of AFM nano-indentation stiffness. We conclude that the possible alterations previously found in aneurysmal SMCs do not affect significantly the AFM nano-indentation stiffness of their cytoskeleton.
[DOI: 10.1115/1.4053657]

Keywords: cell biomechanics, ascendant thoracic aortic aneurysm (ATAA), mechanotransduction, smooth muscle cells (SMC), fluorescent microscopy (FM), atomic force microscopy (AFM), nanoindentation

1 Introduction

Aortic smooth muscle cells (SMCs) are known to be very sensitive to their micro-environment. Under physiological conditions, mature SMCs remain quiescent and partially contracted, maintaining a basal tone which contributes to stress homeostasis in the aortic wall [1–6]. Within pathologies such as ATAA, genetics [7–15], hemodynamics [16,17] or biomechanics [8,18,19], clearly influence the cell phenotype, namely, proliferation, migration, and synthesis of extracellular matrix (ECM) components, or even apoptosis [1,2,4,5,20–22]. The fraction of SMCs with a synthetic phenotype tends to increase at the expense of SMCs with a contractile phenotype [1–3,19,23–27], which results in tissue remodeling [1,24,28,29]. During remodeling, SMCs synthesize collagen fibers to reinforce the media layer of the aortic wall [1,5,30]. However, the induced permanent stiffening can make the aortic wall more vulnerable to rupture [16,18,26,31,32].

Although the effects of these changes are more and more well-known at the tissue level, they remain unclear at the subcellular level. In fact, SMCs sense their environment thanks to specific mechanoreceptors that induce complex chain reactions [7,14,20,26,33,34]. Synthetic SMCs are less responsive to vasoactive stimuli and cannot contribute to mechanotransduction as actively as contractile SMCs [5,7,13,19,22,30,35–37].

Atomic force microscopy (AFM) is a scanning microscopy technique [38,39] providing nanometer-scale imaging of biomolecular interactions in the cell membrane and its cytoskeleton [40,41]. Thanks to its assets, AFM has become commonplace in cell biomechanics [42–45]. Standard AFM modes for mechanical

investigation are based on nano-indentation, by achieving at least one approach-retraction cycle of the tip onto the sample surface and by recording the corresponding tip deflections. Nano-indentation was previously used in single-point and successive measurements on a single cell [6,46–50]. For successive measurements and corresponding nanomechanical mapping, novel AFM modes were recently developed. They extend the traditional force-volume mode that operates in quasi-static. For instance, the Peak-Force^{TM} and Quantitative Imaging^{TM} (QI^{TM}) modes operate a sinusoidal motion, which allows intermittent contact between the tip and the sample surface [51,52]. However, since AFM is a contact technique, subcellular characterization, as, for instance, exploration of the actin network in the cytoskeleton, requires to adjust the applied force (i.e., the setpoint) in order to induce deformations of the cell components under the membrane without damaging the cell [53,54].

Atomic force microscopy nano-indentation was seldom used to characterize aortic SMCs or their surrounding extracellular matrix. It was reported that SMCs have an increased stiffness in case of hypertension [55], aging [56,57] and Marfan Syndrome [6]. It was also shown that cell stiffness and adhesion are increased with vasoconstrictor agonist Angiotensin II [58] or intracellular concentration of calcium ions [50]. Using AFM indentation with a large tip at the tissue level and a sharp tip at the fiber level, it was found that the aortic wall micro-architecture is stiffer and interconnections between ECM fibers are missing in case in ATAA [59]. However, these previous studies never achieved subcellular characterization in the cytoskeleton of living aortic SMCs.

Moreover, we recently found that primary SMCs of aneurysmal aortas apply larger traction forces than primary SMCs of healthy aortas [27]. We explained this result by the increased abundance of hypertrophic SMCs in aneurysmal aortas. This was initially

---

Table 1   AFM tip reference and characteristics

Experiment	Tip reference	Radius of curvature	Spring constant k
Cells on gel A	HQ:CSC17/Cr-Au BS	8 nm (uncoated)	0.21 N/m
Cells on gel B	HQ:CSC17/Cr-Au BS	8 nm (uncoated)	0.26 N/m
Empty gels (A and B)	HQ:CSC17/Cr-Au BS	8 nm (uncoated)	0.30 N/m

thought to result from the phenotypic switch from contractile to synthetic SMCs, the latter being bigger due to the development of their synthetic organelles [60]. However, a larger variety of phenotypic modulations have recently been introduced, questioning the duality between "contractile" and "synthetic" phenotypes, and highlighting other important phenotypes in aortic diseases, such as osteogenic [61] or degradative [62] SMCs.

The effects of these phenotypic variations on the cytoskeletal stiffness have never been investigated. It is well known that cell stiffness is altered in cancer [63]. But the effect of aneurysm on SMC stiffness still needs to be clarified [57]. *Crosas-Molist* et al. [6] found that Marfan VSMC were stiffer than control cells, but there is a pressing need to clarify if stiffness variations may potentially arise in SMCs from idiopathic aortic aneurysms.

In this study, we address this need using AFM nano-indentation on individual living human aortic SMCs for the first time, from healthy and aneurysmal lineages, and derived regional variations of their cytoskeleton stiffness.

After describing the methodology, we report the measured force–displacement curves and the deduced maps of stiffness parameters across the cytoskeleton of 11 control healthy SMCs and 10 aneurysmal SMCs adhering on substrates with the same elastic modulus, and 15 healthy SMCs adhering on stiffer substrates. We finally discuss the obtained results with respect to the cytoskeletal biomechanics and tensional state.

2   Material and Methods

2.1   Healthy and Aneurysmal Cell Lineages. Two types of SMCs were used for this study:

(1) A commercial human AoSMC lineage from the primary culture of a healthy aorta from a 30-year-old female donor was purchased from Lonza (Verviers, Belgium) at passage 3. The cells were cultured for initial proliferation in a growth medium (SmGM-2, Lonza). Then, we stored the AoSMCs at passage five into liquid nitrogen. In each aliquot, about 3×10^6 cells remained in 1.5 mL of a freezing solution containing 10% fetal bovine serum, 10% dimethyl sulfoxide as a cryoprotectant, and 80% SmGM-2 complete medium.

(2) The aneurysmal lineage was developed in our laboratory [27]. AnevSMCs were extracted from an ATAA tissue collected after informed consent during surgical aneurysm repair. The aneurysmal lineage called AnevSMC was extracted from a 69-year-old male patient [27]. Several aliquots of each aneurysmal lineage at passage 2 were stored in liquid Nitrogen.

After thawing, the cells were transferred into a T-75 flask for an entire week in growth medium (SmGM-2, Lonza). Incubating the culture dishes at 37 °C and 5% CO_2 is necessary to maintain the pH at 7.2–7.4. Then, the SMC were cultured one week more in a basal medium (SmBM, Lonza), containing low (2%) fetal bovine serum and 0.04% heparin, according to the manufacturer's instructions in order to preserve a contractile phenotype. Once they reached 70–80% confluence, we used a standard cell detachment protocol using a trypsin treatment with a low trypsin – ethylenediaminetetraacetic acid solution (0.025% Trypsin and 0.75 mM ethylenediaminetetraacetic acid (1X), Sigma, Saint Quentin Fallavier, France) to break down the focal adhesions in the culture dish without damaging the cells. Then, the cells in

suspension could be used for subculturing or for sample preparation. In our study, AoSMCs were seeded onto the sample surface at passages 5–6 and AnevSMCs at passages 3–4.

2.2   Sample Preparation and Staining. For further comparison with AFM images and localization of the cell components under the membrane, we imaged the cell internal architecture with fluorescent microscopy. We used fluorescent staining on fixed AoSMCs adhering to collagen-coated hydrogels. We stained the filamentous actin (F-actin), focal adhesions (vinculin), and alpha smooth muscle actin (α-SMA), the latter being specifically expressed by SMCs.

For each AFM measurement campaign, one aliquot of both Ao- and Anev- SMCs was previously cultured in conditions promoting the development of SMC contractile apparatus (as explained in Sec. 2.3). Then, the cells were seeded in Petri dishes made of plates containing commercial hydrogels (Cell Guidance System, PetriSoft™ 35, collagen precoated). We used two different hydrogels from cell guidance system: gel A (softer gel with an elastic modulus of 12 kPa according to the supplier) and gel B (stiffer gel with an elastic modulus of 25 kPa according to the supplier). As the gel softness/stiffness may slightly evolve with time, we assessed it again with AFM on the supplied gels without cells (Appendix E available in the Supplemental Materials on the ASME Digital Collection).

In order to assess the influence of both disease (ATAA) and substrate stiffness on the subcellular stiffness, we considered three groups for this study, namely,

(1) AoSMCs on gel A (Group 1),
(2) AnevSMCs on gel A (Group 2),
(3) and AoSMCs on gel B (Group 3).

Our previous studies on SMCs showed that AoSMCs apply maximum traction forces on gel A [27]. These hydrogels were made of a 400-μm-thick layer of polyacrylamide, with a type I collagen coating added during the manufacturing process that provides a physiological surface for cell adhesion and culture. An amount of 50,000 cells were seeded in each well and incubated in basal medium for two days before AFM nano-indentation experiments. This duration was sufficient to ensure that SMCs spread and apply maximal tractions.

2.3   Atomic Force Microscopy Indentation of Individual SMCs in Liquid. We used a JPK Nanowizard® 3 AFM (JPK Instruments, Berlin, Germany), equipped with a heating stage (HTHS™) that is set at 37 °C, and JPK Data Processing software (V.6.1.118). We calibrated HQ:CSC17/Cr-Au BS (MikroMasch Europe, Wetzlar, Germany) probes before our AFM measurements (Table 1). We also chose an uncoated tip having a significantly lower radius of curvature (8 nm), which increased the lateral resolution for AFM images.

Due to the limited volume accessible with the AFM tip (approximately $30 \times 30 \times 6.5$ μm^3), we paid particular attention to the choice of the scan area (region of interest: ROI). SMCs were averagely 200–300 μm long and 5–10 μm wide. We chose the ROI far enough from the SMC nucleus, in order to limit the variations of height. We chose similar ROIs for all the cells, always considering an area taking into account one of the extremities of each cell. This also permitted to investigate regions near focal adhesions, which are known to play an important role in mechanotransduction [34].

Table 2 Setpoint values (F, in nN) for each indented cell from the different groups: (a) AoSMCs adhering on gel A, (b) AnevSMCs adhering on gel A, and (c) AoSMCs adhering on gel B

F	1	2	3	4	5	6	7	8	9	10	11	12	13	14	15
A	2	3	3	3	3	3	3	3	3	3	3				
B	2	2	2	3	3	3	3	3	2	4					
C	5	3	3	5	5	3	3	3	3	5	4	5	3	3	5

Table 3 Total number of nano-indentation points for the two cell lines and for empty gels

	AoSMC	AnevSMC	Empty gels
Gel A	11 cells 220,279 points	10 cells 206,915 points	2 gels 158,464 points
Gel B	15 cells 382,292 points	—	2 gels 147,456 points

Once removed from the incubator, the Petri dishes containing our cell cultures were stored in a portable incubator (Darwin Chamber, NQ09P, Saint-Louis, MO) set at 37 °C in order to maintain the temperature constant during transport until the AFM platform and until the equipment was set to the right parameters. The purpose was to minimize the experiment duration and to avoid cell damage. The Petri dish was also maintained at 37 °C. We added a drop of medium on the AFM probe before approaching it to the sample until the drop and the bath create a meniscus. We first performed a soft approach by engaging the tip using the standard automatic process. Once the engagement was achieved, we withdrew the tip and moved the sample in order to select the ROI.

At every point across the ROI, we employed the QI mode to assign vertical motions of the AFM tip and to measure the vertical force resulting from the elastic response of the nano-indented surface. We found that a maximum setpoint of 5 nN was needed in order to avoid damaging the cell and a minimum setpoint of 2 nN was needed to induce a sufficient deformation of the cytoskeleton. The precise setpoint values for each investigated cell are given in Table 2. The setpoint is the reference force for both height (topography image) and indentation depth. It is the maximal applied force: once the setpoint is reached while indenting the surface, the AFM tip is retracted. The size of the ROI (30×30 μm) was always set to 30×30 μm^2. We increased progressively the image resolution from 128×128 points (low resolution mapping) to 256×256 (for high-resolution mapping). The indentation speed was set at 200 or 250 μm/s in constant speed configuration.

2.4 Mechanical Model of the Indented Cell. Although the cell is heterogeneous, we simply derived an apparent contact stiffness at every nano-indentation point, which merged the contribution of both the membrane and the cytoskeleton in a structural stiffness parameter. Deriving local material stiffness parameters of the different cell compartments would require inverse methods, which are discussed in Sec. 4.3.

To derive the local apparent indentation stiffness, we used the Sneddon contact model between a cone and an elastic half-space [64]. We assumed that the cell has a linear elastic behavior with negligible adhesive interactions between the AFM tip and the cell in liquid [43,64]. The cell was also assumed as incompressible, similar to soft gel-like materials [65]. More details about the theory can be found in the work of *Sirghi* [47].

The position z of the tip is first converted into an indentation depth δ such as

$$\delta = z - \frac{F}{k} \tag{1}$$

where $\frac{F}{k}$ represents the probe deflection due to the applied force F, and k is the spring constant of the cantilever. This operation is automatically performed by the JPK data processing software.

The eventual relationship between F and δ according to the Sneddon contact model is

$$F = \frac{2}{\pi} \frac{E}{(1 - \nu^2)} (\tan\alpha) \delta^2 \tag{2}$$

where ν is the Poisson's ratio ($\nu = 0.5$), α is the half-angle of the tip ($\alpha = 20$ deg for a HQ:CSC17 tips) and E is the "apparent" stiffness of the cell.

By adjusting the indentation curve obtained experimentally with Eq. (2), we obtained the apparent stiffness at every indented point of the ROI. This adjustment was achieved with a standard least squares method, which minimizes the sum of squares of errors at all the N time points throughout force application, according to

$$S(E) = \sum_{i=1}^{N} \left(F_{\text{exp}}(\delta_i) - F_{\text{mod}}(\delta_i; E) \right)^2 \tag{3}$$

where F_{exp} is the measured force and F_{mod} is the calculated force for the same δ. The solution is obtained by minimizing $S(E)$ such as

$$E = \frac{\pi(1 - \nu^2)}{2\tan\alpha} \left(\frac{\sum\limits_{i=1}^{N} \delta_i{}^2 F_{\text{exp}}(\delta_i)}{\sum\limits_{i=1}^{N} \delta_i{}^4} \right) \tag{4}$$

2.5 Data Processing. The force–displacement curves obtained at each measurement point were used to reconstruct two maps: a map of the height when the setpoint force is applied (called further the topography map) and a map of the local apparent stiffness (called further the stiffness map). The procedure was performed on 11 AoSMCs adhering onto gel A, 10 AnevSMCs adhering onto gel A, and 15 AoSMCs adhering onto gel B. The total number of measurements is reported in Table 3. Supplemental data were acquired on empty gels (gel A and gel B) to verify their stiffness values (Appendix E available in the Supplemental Materials on the ASME Digital Collection).

In order to reconstruct the topography and the stiffness maps, the 256×256 (128×128 for the empty gels) raw force–displacement curves across the scanned area were processed with the JPK SPM software, using a program called "Hertz fit," which consists of the following steps:

- Adjustment of the sensitivity and spring constant of the tip (calibration step described in Sec. 3.3).
- Selection and adjustment of the baseline (adjustment of the Y-axis offset). The function automatically calculates the average value of the selected area (by user), and subtracts this from the whole curve (Fig. 1).
- Determination of the contact point: adjustment of the X-axis offset. The function automatically calculates the point where the force curve crosses the baseline and sets this as the zero of the X-axis.

Table 4 Parameters of the lognormal distribution for the three individual SMCs shown in Fig. 2

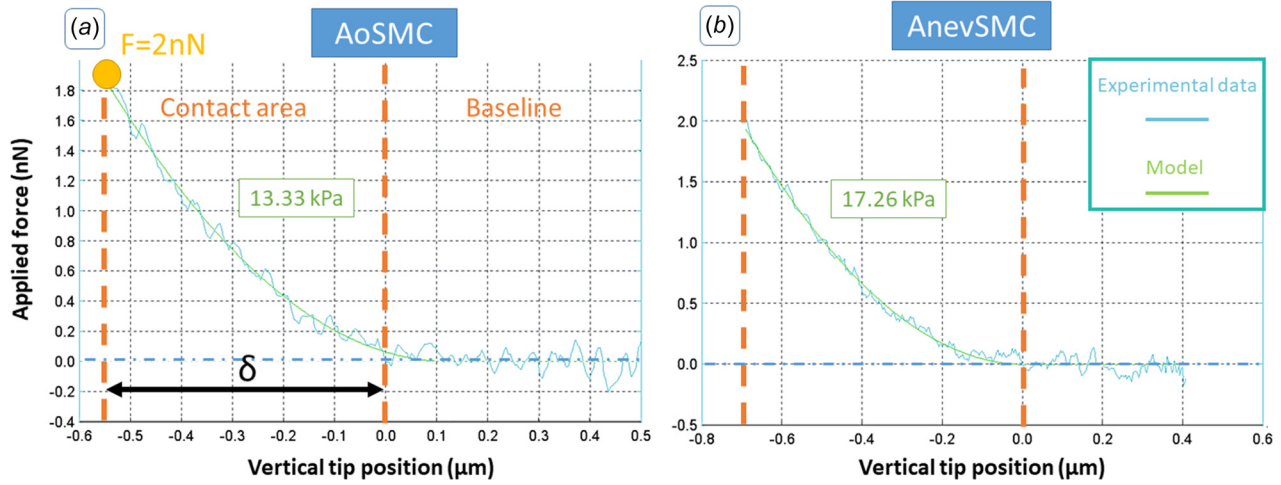|	μ	σ
AoSMC, Gel A	2.82	0.58
AnevSMC, Gel A	2.88	0.31
AoSMC, Gel B	3.05	0.38

Fig. 1 Force curves obtained from the indentation experiments on AoSMC (*a*) and AnevSMC (*b*). The experimental data is fitted with the Sneddon model. These curves were obtained at a point of the corresponding AFM images representing the apparent stiffness parameter. The corresponding apparent stiffness value is written in a box on each graph. The maximal applied force F (setpoint) is 2nN. The δ parameter is the maximum indentation depth reached at the setpoint force of 2nN, which is used to reconstruct the topography maps (Figs. 3(*e*) and 3(*f*)). The baseline corresponds to the contactless part of the force curve: it is used to define the zero of the *Y*-axis.

- Calculation of the vertical tip position by subtracting the cantilever deflection to the scanner height according to Eq. (1)
- Determination of the local apparent stiffness E according to Eq. (4).

Although these steps are automatic, we checked if the force–displacement curves were correctly adjusted. Each curve consisted of a baseline representing the origin of the *Y*-axis where the force remains null, and a contact area (between the vertical dotted lines on Fig. 1), where the force increases with the indentation depth, until the maximal applied force (the setpoint of 2nN, represented by the point at the top of the curve, in the upper left corner on Fig. 1(*a*)). After deriving the apparent stiffness parameter according to Eq. (4), the force–displacement curve predicted by the model was deduced (the smooth curve giving the trendline of the experimental data in Fig. 1).

After completing the derivation of the apparent stiffness and baseline height at every point of the ROI, the results were exported as JPK data files, which can be opened in JPK SPM or GWYDDION software for further processing. We eventually applied a background correction removing some punctual defects. For that, we fitted a plane (linear in our case) to the selected area and subtracted this from the measured data to detect these defects. Another function called "remove lines" was also useful for correcting the lines where the tip sticked to the surface and then pulled off, leaving streaks in the image. This function replaced the selected lines by the average of the neighboring scan lines. After these cleaning procedures, data (arrays of baseline heights and apparent stiffness values) were eventually exported to MATLAB for statistical analyses and figure creation.

In MATLAB, a filter was applied to separate points belonging to the gel and points belonging to the cell. For that, we applied two successive thresholds on both height and measured stiffness. More precisely, the points belonging to the gel were defined as points with a baseline height below 1 μm and an apparent stiffness below 25 kPa for gel A and below 50 kPa for gel B. After separation of the gel and cell areas across the ROI, we processed separately the height and stiffness values of each area to display histograms and perform statistical analyses.

Histograms, which represent the distribution of the apparent stiffness values, consisted of 100 bars equally distributed over the range 0-45 kPa. The median value was reported as a vertical line on these histograms.

2.6 Statistics. For each cell, we derived the median value of the stiffness properties. The medians obtained for each cell were grouped into group 1 (AoSMCs on gel A), group 2 (AnevSMCs on gel A), and group 3 (AoSMCs on gel B). Each group was represented as a boxplot in MATLAB. To compare the groups, we performed a statistical analysis consisting in using the nonparametric Mann–Whitney test based on the null hypothesis of equal medians between two groups. A *p*-value under 0.05 indicates that the test rejects the null hypothesis at the 5% significance level.

We also represented the distributions of apparent stiffness values as histograms in MATLAB. We inferred that the logarithm of the apparent stiffness, denoted E, is normally distributed, meaning that the distributions satisfy a lognormal distribution, which may be written such as:

$$P(E) = \frac{1}{E\sigma\sqrt{2\pi}}\exp\left(-\frac{(\ln(E) - \mu)^2}{2\sigma^2}\right) \quad (5)$$

where μ is the mean of $\ln(E)$, σ is the standard deviation of $\ln(E)$ and $P(E)$ is the probability distribution. Note that for a lognormal distribution with parameters (μ, σ), the mean of E is e^μ and the standard deviation is $\sqrt{(e^{\sigma^2} - 1)e^{2\mu + \sigma^2}}$.

For each cell and for each group, we derived the coefficient of determination R^2 in order to measure the strength of the lognormal distribution in approximating the stiffness distributions.

Eventually, given the lognormal distributions and their parameters, we estimated the probability $P(E_2 > E_1)$ that cells of group 2 have a larger stiffness than cells of group 1, and the probability $P(E_3 > E_1)$ that cells of group 3 have a larger stiffness than cells of group 1, using the following expression:

$$P(E_j > E_i) = \frac{1}{2}\left[1 + \text{erf}\left(\frac{\mu_j - \mu_i}{2\sqrt{\sigma_i^2 + \sigma_j^2}}\right)\right] \quad (6)$$

where μ_i and μ_j are the expected value or mean of $\ln(E_i)$ and $\ln(E_j)$, σ_i and σ_j are the expected value or mean of $\ln(E_i)$ and $\ln(E_j)$ and erf is the error function defined such as:

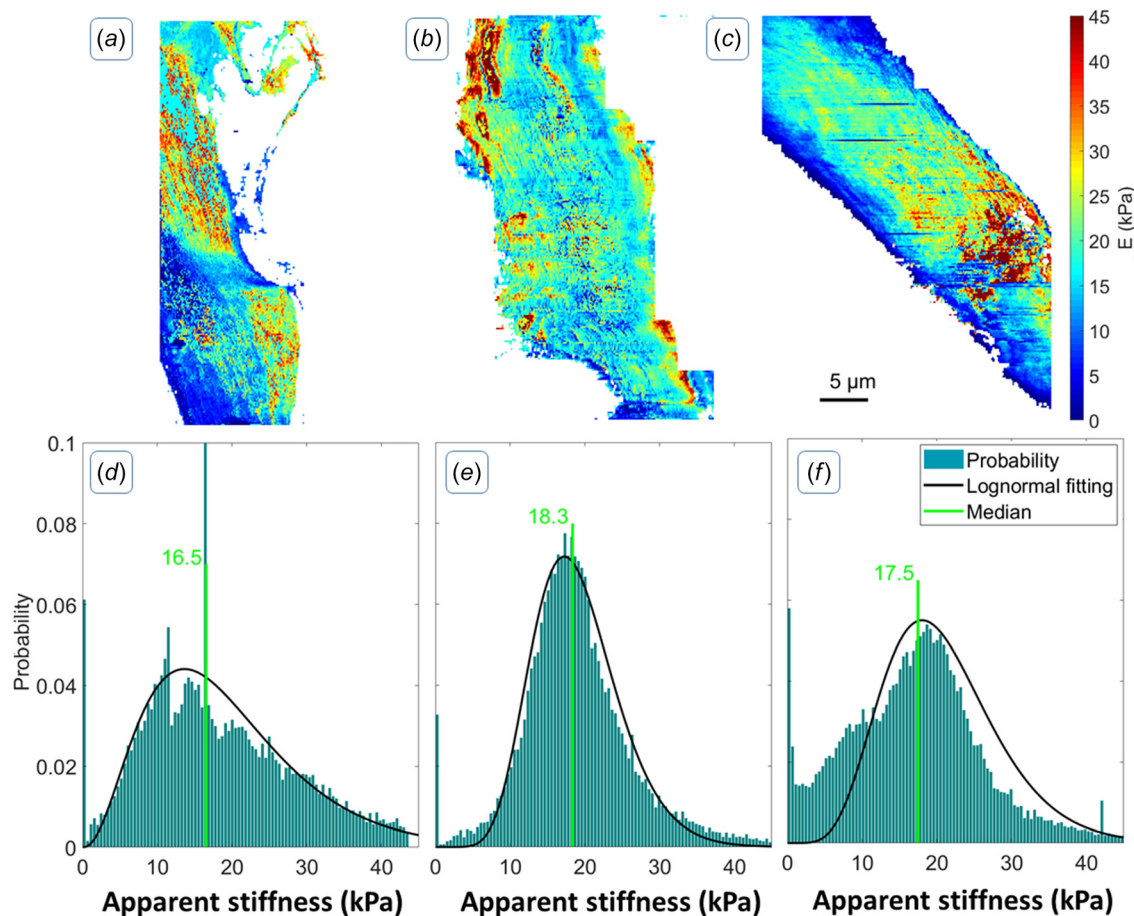$$\text{erf}(z) = \frac{2}{\sqrt{\pi}}\int_0^z \exp\left(-\frac{t^2}{2}\right)dt \quad (7)$$

Fig. 2 Apparent stiffness maps and corresponding histograms for an isolated AoSMC (*a* and *d*) (setpoint 2nN, speed 200 μm/s, 38,712 points) and AnevSMC (*b* and *e*) (setpoint 4nN, speed 250 μm/s, 30,688 points) on gel A, and AoSMC (*c* and *f*) on gel B (setpoint 4nN, speed 250 μm/s, 34,933 points). In (*f*), the first values until $x = 8.77$ (equivalent to the first 20 bars) were removed to obtain the lognormal fitting. Stiffness range: 0–45 kPa, 100 bars. The median values are shown with vertical lines. The bold line curve represents the regression with a lognormal distribution (Parameter values are given in Table 4). The full set of data is reported in Appendix B available in the Supplemental Materials on the ASME Digital Collection.

$P(E_j > E_i)$ is an estimation of the confidence interval that the assumption $E_j > E_i$ is reliable. A confidence interval of 95% is quite standard. Eventually, given the variance of the distribution functions obtained in our experiments, we deduced the minimum difference between the means of two groups e^{μ_i} and e^{μ_j} that corresponds to the 95% interval.

3 Results

3.1 Comparison of the Stiffness Distributions

- Stiffness distribution across single cells

In Fig. 2, we show the distribution of apparent stiffness of a representative cell of each group (group 1 in Figs. 2(*a*) and 2(*d*), group 2 in Figs. 2(*b*) and 2(*e*), group 3 in Figs. 2(*c*) and 2(*f*)). The distributions look similar whatever the lineage and the substrate stiffness. Nevertheless, the whole set of data given in Appendix B and C available in the Supplemental Materials on the ASME Digital Collection reveals a high variability between cells from the same group in terms of median apparent stiffness values. The lognormal distribution shows a good agreement with these distributions of apparent stiffness values. The full statistical analysis including individual median values and the parameters of the lognormal distribution are reported in Appendix C available in the Supplemental Materials.

- Differences between the different groups of cells

The median value for each cell is reported in Appendix C (Table C1) available in the Supplemental Materials, whereas the means and standard deviations are reported in Tables C2 and C3 available in the Supplemental Materials, respectively.

The statistical test revealed that there were no significant differences between the medians of the three groups (Appendix C, Fig. C1 available in the Supplemental Materials).

For each group of cells, we pooled off the obtained stiffness values together in order to obtain the complete distribution of values across the whole group as a histogram. Results are shown in Fig. 3. The lognormal function shows a very good agreement with these distributions of apparent stiffness values, with R^2 values ranging from 0.64 to 0.88, as reported in Table 5. The distribution of group 2 is the one deviating the most from the lognormal distribution, with $R^2 = 0.64$, mostly because of several secondary peaks in the histograms in the range 15–25 kPa (Fig. 3).

From these distributions, it appears clearly that there is a slight increase of stiffness in group 2 (aneurysm cells) compared to the two other groups. The probability that cells of group B have a larger stiffness than cells of group A is $P(E_2 > E_1) = 0.61$. Therefore the confidence interval of the assumption that aneurysmal SMCs are stiffer than healthy ones is only of 61%. The probability that cells of group 2 have a larger stiffness than cells of group 1 is $P(E_2 > E_3) = 0.62$ and the probability that cells of
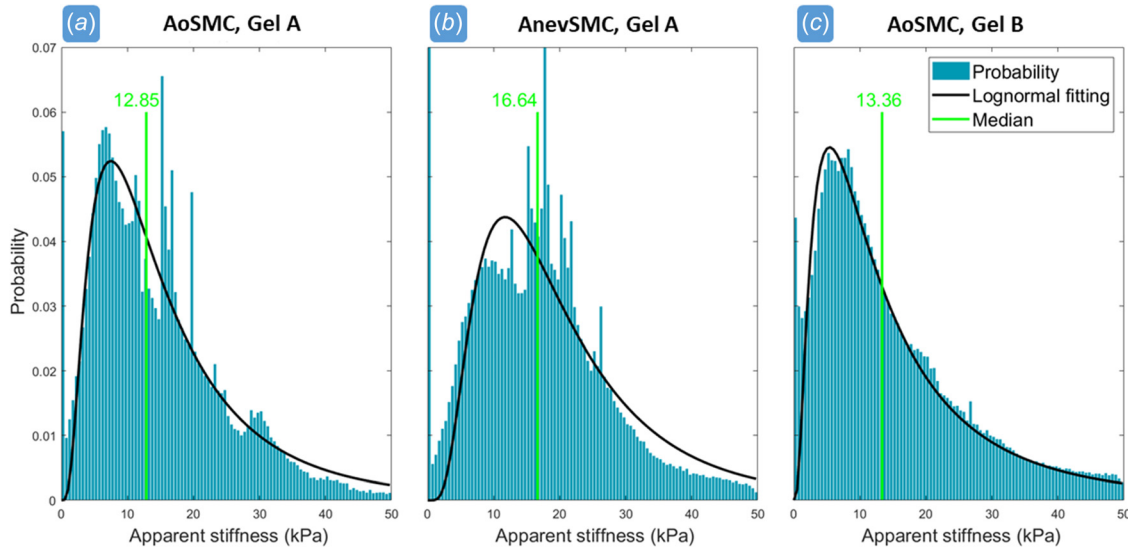
Fig. 3 Histograms showing the distribution of the apparent stiffness values measured on the whole population of cells from both Ao- (*a*) (*N* = 11, 220,279 points) and Anev- (*b*) (*N* = 10, 206,915 points) SMCs on gel A and AoSMCs on gel B (*c*) (*N* = 15, 382,292 points). The bold line curve corresponds to the best-fit lognormal distribution (Parameter values are reported in Table 5). The vertical line indicates the median value. Stiffness range: 0–45 kPa, 100 bars.

group 3 have a larger stiffness than cells of group 1 is only of $P(E_3 > E_1) = 0.52$.

Moreover, the standard deviations reported in Table 5 for each group (and even in Table C2 available in the Supplemental Materials on the ASME Digital Collection for each cell) are relatively large. We estimate that, given standard deviations of about 15 kPa as reported for group 1 and 2 in Table 5, the 95% confidence interval could only be reached when the means of two groups are separated by at least 30 kPa. Such a difference is much larger than the maximum difference between means of group 1 and 2. Interestingly though, there are only a couple of cells in group 3 showing means above 35 kPa, but they usually correspond to distributions with larger standard deviations.

3.2 Localized Differences of Apparent Stiffness Values

- Apparent stiffness maps

The obtained stiffness maps revealed heterogeneities across each cell. For instance, the structure under the membrane is clearly visible, showing the trace of stress fibers, in the apparent stiffness mapping (Figs. 4(*c*) and 4(*d*)). The structure is even revealed with a higher contrast than topography maps (Figs. 4(*e*) and 4(*f*)). Interestingly, the AFM images of the given AoSMC show a lamellipodium-like substructure on the thinnest region (upper region on Figs. 4(*c*)–4(*e*)). We also noticed a stiffer and uniform layer around the AnevSMC (Fig. 4(*d*)). The full set of data are shown in Appendix A available in the Supplemental Materials.

We also report in Appendix E available in the Supplemental Materials the distribution of stiffness obtained on empty gels, without cells. The median stiffness value measured on gel A was 15.9 kPa and the median stiffness value measured on gel B was 25.7 kPa. The obtained values were close to the ones indicated by the gel supplier (12 kPa for gel A and 25 kPa for gel B). There is again a relatively large scattering in the stiffness values. The scattering of the stiffness values in the gel is clearly an effect of the very high spatial resolution of stiffness measurements with our 8 nm-AFM tip. The porous structure of the gels can even be detected in the AFM stiffness and topography maps, as shown in Fig. E2 available in the Supplemental Materials.

- Multiple peaks

As previously noticed, local variations of the stiffness (variations with a high spatial frequency) show undulations, which may be related to the underlying stress fibers, whose pattern is shown in the fluorescent microscopy images of Fig. 5.

There are also spatial variations of the measured stiffness for points which are separated by larger distances. These variations at low spatial frequency (Fig. 2 and Appendices A and B available in the Supplemental Materials), manifesting with relatively large areas of lower or stiffness, also manifest in the histograms with distinct spikes. Most of the histograms of apparent stiffness values appear to be multimodal. In Appendix D available in the Supplemental Materials, we show the results of a supplemental analysis where we separated the contribution of each secondary spike in the images. Although the multimodality may be attributable to structures appearing sometimes in the images themselves, it was not possible to identify specific patterns related to these local structures if Figs. D2 and D3 available in the Supplemental Materials. The difficulty of separating precisely the contribution of each local structure can be explained by the superimposition of the high spatial frequency variations and scattering, as discussed previously, onto the low spatial frequency variations. Moreover, the stiffness in different regions of the cell was measured several minutes apart, as acquiring the whole AFM scan takes more than 30 min. Therefore, the spikes in the histograms may also be induced by remodeling effects during the AFM scanning time.

- Cytoarchitecture

Fluorescent imaging of cells from both cell lineages showed that the SMC cytoskeleton is composed of a complex fibrous network (Fig. 5). The actin network is particularly dense in the lamellipodium near the focal adhesions of the cell, and forms long stress fibers linking focal adhesions together or linking focal adhesions to the nucleus. A crisscrossed arrangement of actin fibers was noticed in the lamellipodium, both for the AnevPrim (Fig. 5(*b*)) and the AoSMC lineage (Fig. 5(*a*)). Conversely, in lateral regions, the actin stress fibers were closer and parallel to each other, forming thick bundles at each side of the cells.
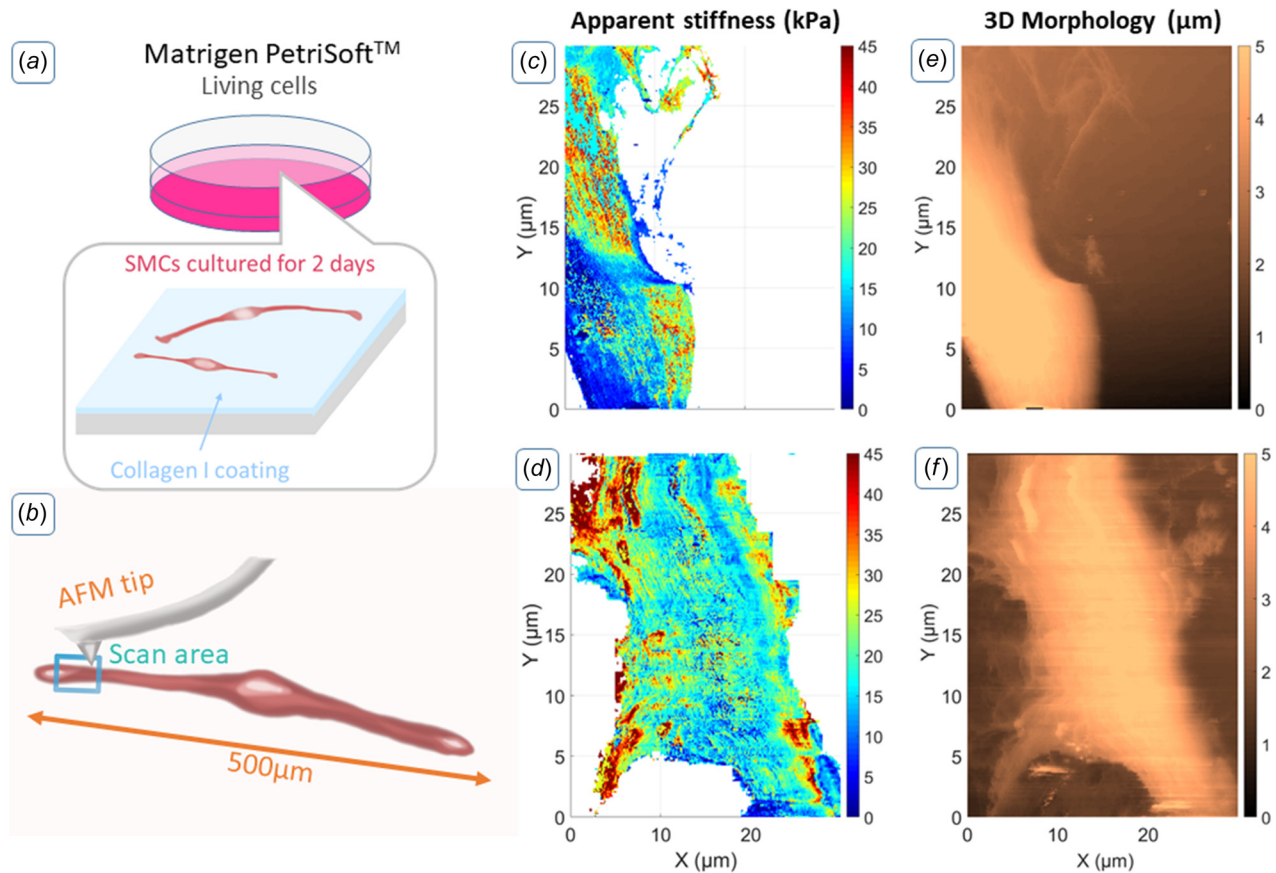
Fig. 4 The Matrigen 35 mm Petri dishes contains a collagen I precoated hydrogel, on which SMCs adhere naturally after seeding (a). The tested stiffness values are 12 kPa (gel A), and 25 kPa (gel B). A scan area was chosen close to the tip of individual SMCs (b). AFM apparent stiffness maps (c and d) and topography maps (e and f) for an isolated AoSMC (c) (256 px/30 μm, setpoint 2nN, speed 200 μm/s) and AnevSMC (d) (setpoint 4nN, speed 250 μm/s) adhering on a 12 kPa collagen-coated hydrogel. The full set of data is given in Appendix A available in the Supplemental Materials on the ASME Digital Collection.

4 Discussion

Aortic SMCs play a vital role in maintaining mechanical homeostasis in the aorta. We recently found that SMCs of aneurysmal aortas apply larger traction forces than SMCs of healthy aortas [27,66]. We explained this result by the increased abundance of hypertrophic SMCs in aneurysmal aortas. In this study, we have investigated whether the cytoskeleton stiffness of SMCs may also be altered in aneurysmal aortas. For that, we have characterized for the first time the local apparent stiffness distribution across the cytoskeleton of human aortic primary SMC (healthy and aneurysmal origin) using AFM nano-indentation. Previously, AFM was rarely used to characterize aortic SMCs or their surrounding extracellular matrix [6,55–57]. We found that the obtained stiffness distributions were globally lognormal, with a slightly higher mean in aneurysm cells. However, the differences were not statistically significant due to the very large dispersion of the AFM nano-indentation stiffness.

There may be different reasons explaining the large dispersion. One reason is that, given the large strain rates used in our measurements (above 100 Hz), the measured apparent stiffness may actually be a combination of an actual elastic modulus and a viscous component. Previous work showed that soft biological objects behave like stiff materials while they undergo a high-frequency excitation [67,68]. Caporizzo et al. [69] studied the effect of strain rates on the apparent stiffness of fibroblasts measured with AFM indentation. They found a stiffness of 2.5 kPa at 0.1 Hz, and a stiffness of 4 kPa at 100 Hz. Therefore, based on their study, we may approximate that the stiffness in our experiments is about two times larger than the stiffness at 0.1 Hz. In the work of Nawaz et al. [70], it was also found that the stiffness

increased of about a factor 2 between low and high deformation rates. This depended though on the magnitude of the deformation. They found that at low indentation ($<0.2\,\mu$m) the cell showed an almost ideal elastic response, whereas at larger indentation the measured cell stiffness depended more significantly on the loading rate. The contribution of the viscous component to the apparent stiffness obtained in our study should be determined in the future in order to derive the actual elastic modulus and determine its variations across the cell and between different cell lineages. However, it is important to note that the rate effects did not appear to affect the mean stiffness of the gels without cells (Appendix D available in the Supplemental Materials), as we found similar elastic moduli as the ones provided by the supplier.

Another cause of dispersion in the stiffness maps may be related to the time needed for acquiring an image with the QI mode. In fact, due to possible remodeling during the scanning time, AFM scans do not represent any particular state of a cell at a given time. Only the very local variations of the stiffness (variations with a high spatial frequency, i.e., between very close points where the stiffness was assessed almost simultaneously) may show variations related to the underlying structure. For instance, we see clear undulations that may indicate the underlying fibrous structure as it appears in fluorescent microscopy images of Fig. 5. However, for points that are separated by larger distances, hence where the stiffness was assessed at times of several minutes apart, the observed differences of stiffness may be induced by remodeling effects.

One of the manifestations of data dispersion was the multimodality of the histograms, with spikes suggesting the possible presence of different cell structures. We tried to localize the stiffness
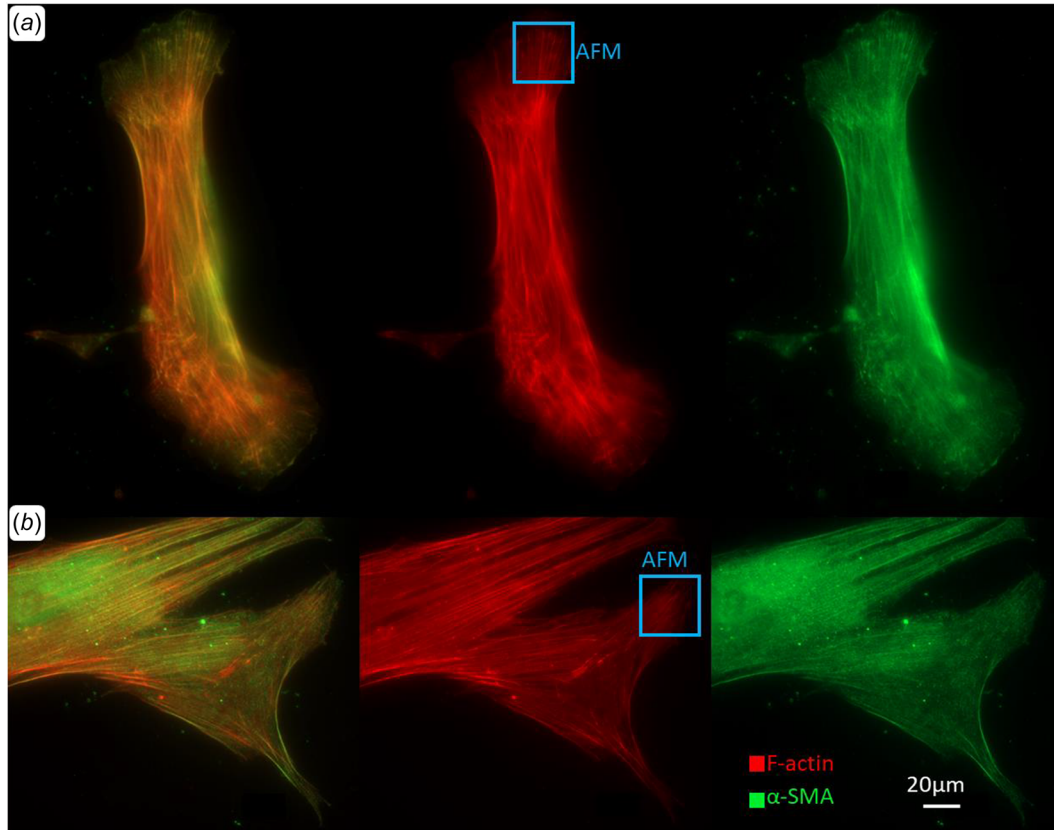
Fig. 5 Fluorescent microscopy images of fixed Lonza AoSMC (M, 43 y.o.) (*a*) and AnevPrim (*b*). Observation of cell internal architecture in terms of cytoskeletal structure. The fluorescent channels are: DsRed (F-actin) and green fluorescent protein (α-SMA). Channels are displayed on the figure as follow (left to right): all channels - DsRed - green fluorescent protein. Microscope Axio Observer.Z1/7, Objective: Fluar 40×/1.30 oil. The square shows the typical AFM scan area chosen for each cell of this study.

values corresponding to each peak in Appendix D available in the Supplemental Materials on the ASME Digital Collection. However, when extracting the local spikes, it was not possible to identify specific patterns related to these local structures. The mechanobiological meaning of these spikes in terms of specific cell structures requires further investigations. It may also be related to the time variations discussed above.

Although our previous study revealed a hypertrophy of AnevSMCs [27], differences of stiffness values between AnevSMC and AoSMC were not statistically significant (Fig. 3). Both fluoroscopic and AFM imaging also tended to show that aneurysmal and healthy cells present globally the same local cytoarchitecture (Fig. 5). These local assessments should be complemented in the future by more global assessments of the cell stiffness along the long axis, which could be achieved using microbiaxial stretching [71].

A previous study using punctual nano-indentation on monkey aortic SMCs showed that stiffness values of SMCs from young monkeys are in the 10–40 kPa range, which is similar to the stiffness values of healthy human SMCs, for similarly applied force between 1 and 5 nN [57]. Another study using AFM indentation on SMCs of Marfan patients showed an increased stiffness, both in the cells and in the ECM [6]. It was suggested that there may be a correlation between the stiffness of SMCs and the stiffness of the aortic wall in which they are embedded [72]. Interestingly, healthy cell lines investigated in our study had a median stiffness value of about 12 kPa, whereas the median value of aneurysmal cells was slightly higher. We also found in a previous study that the traction forces of SMCs depend on the stiffness of their substrate, and that the highest traction forces were reached on gels of 12 kPa stiffness [27,66].

Stiffness mapping using AFM indentation is quite common on soft tissues [73–76] but our results are the first using nano-indentation on human SMCs. Larger tips (generally spherical probes of 1 μm–1 mm diameter) are usually employed at the tissue scale. Thinner tips like the one used in our study enable detecting very small variations, such as the undulations shown in Figs. 2–4 or as the porosity of the gels shown in Fig. E2 (Appendix E available in the Supplemental Materials on the ASME Digital Collection). At the tissue scale, a previous study using AFM-based nano-indentation showed that normal mixtures of collagen, elastin, and SMCs in the wall of a nondiseased aorta had a compressive axial stiffness of 18.7 kPa, as measured by Hayenga et al. [77]. Another study of Oie et al. found the axial stiffness of the media (comprising SMCs and collagen fibrils) to be 17.0±9.0 kPa (mean±SD) [78]. However, for atherosclerotic plaques, the median was found to be in a range between 27.5 kPa and 99.2 kPa for the ECM surrounding the fibrous cap and the intimal region, respectively [79]. Moreover, another study of Tracqui et al. using AFM found that cellular fibrotic regions exhibit a mean elastic modulus of 10.4±5.7 kPa, and hypocellular fibrous caps exhibit a mean Young modulus of 59.4±47.4 kPa, locally rising up to ∼250 kPa [80]. Therefore, stiffness increase seems to be specific to diseased vascular tissues, but the stiffness increase likely results from the remodeling of the extracellular matrix and not from the cells themselves. A number of limitations need to be acknowledged.

The AFM nano-indentation curves were processed using the Sneddon model. This resorts to assuming that the cell has a linear elastic behavior and to neglecting the cell viscosity [43]. Stiffness measurements on viscous materials using indentation can be affected by the indentation speed [67,68]. Although the QI mode has a lower (0.5–100 Hz) indentation frequency than other

Table 5 Statistical parameters of the stiffness distributions for each group shown in Fig. 3

	μ	σ	R^2	Mean (kPa)	Variance	Standard deviation (kPa)
AoSMC, Gel A	2.59	0.76	0.80	13.3	250	15.7
AnevSMC, Gel A	2.86	0.63	0.64	17.5	220	14.9
AoSMC, Gel B	2.53	0.91	0.88	12.6	460	21.6

quantitative AFM mapping modes like PeakForce (0.25–8 kHz) [81], the dynamic effects should be investigated in future work, more specifically viscoelastic properties. Moreover, the influence of the substrate under the cell is difficult to determine precisely. The method should be applied in the perinuclear area of the cell as well.

Another important point of discussion is the geometry and dimension of the tip, which is a cone of only radius of curvature our case. Although a very thin tip is essential to detect the local variations, it appears that a larger tip is more suitable at the tissue scale (to estimate the gel stiffness, for instance). Therefore, the variations and dispersion of stiffness properties in the gels shown in the images of Appendix E available in the Supplemental Materials on the ASME Digital Collection, and probably also in the cells themselves, would be smoothed out with a larger spherical AFM probe. Larger spherical probes were widely used for aortic characterization at the tissue scale within the 1–$10\,\mu m$ range for diameter [78,80], but they are usually not adapted to cell indentation.

Testing living cells represents also a major challenge. The imaging time with the QI mode lasted about 20 min in an optimal setting. This is significantly larger than the timescale of dynamic effects undergone by filamentous structures of the cytoskeleton as assembly/disassembly cycles usually last a few minutes [82,83]. Moreover, it was not possible to scan all the cells at the same location, which may induce some extra variability.

Our experimental conditions on gels between 12 kPa and 25 kPa are significantly lower than real tissues which is normally around 100 kPa, and which can be much larger in pathologies like atherosclerosis [84]. Nevertheless, the specific structure of the medial layer is made of lamellar units and SMCs are connected to the elastic laminae by bundles of elastic microfibrils [19,85,86], which may act as compliant springs between stiffer material, and therefore results in a globally more compliant substrate for the cells. Artificial two-dimensional environments may therefore reproduce similar stiffness properties at the focal adhesion sites, but obviously it does not reproduce the specific structure of the SMC micro-environment in the aorta. Considering lamellar three-dimensional environments in future studies is a priority but this will require addressing a number of challenges to develop these environments.

Finally, in spite of the high number of punctual measurements achieved for each cell, only ∼10 to 15 cells were tested in each group. Future work on a larger number of cells should investigate the mechanical properties of the different cell components in order to identify more in details their local mechanical contributions to the cellular functions.

5 Conclusion

We used the recently developed QI AFM mode in order to achieve nanomechanical mapping of isolated living human aortic SMCs. The obtained results are the first reconstructions of the local apparent stiffness values in the cytoskeleton of human aortic SMCs. The main conclusions are that: (1) all SMCs exhibit globally lognormal stiffness distributions, with medians in the range 10–30 kPa, (2) the mean of stiffness distributions is 16 kPa in aneurysmal SMCs and 12 kPa in healthy cells, (3) the differences between healthy and aneurysmal SMCs are not statistically significant due to the large dispersion of AFM indentation stiffness. Further work will try to reconcile local stiffness variations with

traction force variations previously published by our group [27] using subcellular computational modeling of SMCs. We postulate that understanding the mechanical regulation of vascular SMCs will be highly beneficial for future therapeutic developments against cardiovascular diseases.

Conflict of interest

None.

References

[1] Humphrey, J. D., 2002, *Cardiovascular Solid Mechanics*, Springer New York, New York.

[2] Mecham, R. P., and Schwartz, S. M., 1995, *Vascular Smooth Muscle Cell: Molecular and Biological Responses to the Extracellular Matrix (Biology of Extracellular Matrix Series)*, Academic Press, San Diego, CA.

[3] Michel, J.-B., Jondeau, G., and Milewicz, D. M., 2018, "From Genetics to Response to Injury: Vascular Smooth Muscle Cells in Aneurysms and Dissections of the Ascending Aorta," Cardiovasc. Res, **114**(4), pp. 578–589.

[4] Mao, N., Gu, T., Shi, E., Zhang, G., Yu, L., and Wang, C., 2015, "Phenotypic Switching of Vascular Smooth Muscle Cells in Animal Model of Rat Thoracic Aortic Aneurysm," Interact. CardioVascular Thorac. Surg., **21**(1), pp. 62–70.

[5] Thyberg, J., Blomgren, K., Roy, J., Tran, P. K., and Hedin, U., 1997, "Phenotypic Modulation of Smooth Muscle Cells After Arterial Injury is Associated With Changes in the Distribution of Laminin and Fibronectin," J. Histochem. Cytochem., **45**(6), pp. 837–846.

[6] Crosas-Molist, E., Meirelles, T., López-Luque, J., Serra-Peinado, C., Selva, J., Caja, L., Gorbenko del Blanco, D., Uriarte, J. J., Bertran, E., Mendizábal, Y., Hernández, V., García-Calero, C., Busnadiego, O., Condom, E., Toral, D., Castellà, M., Forteza, A., Navajas, D., Sarri, E., Rodríguez-Pascual, F., Dietz, H. C., Fabregat, I., and Egea, G., 2015, "Vascular Smooth Muscle Cell Phenotypic Changes in Patients With Marfan SyndromeSignificance," Aeterioscler., Thromb., Vasc. Biol., **35**(4), pp. 960–972.

[7] Chen, J., Li, H., SundarRaj, N., and Wang, J. H.-C., 2007, "Alpha-Smooth Muscle Actin Expression Enhances Cell Traction Force," Cell Motil. Cytoskeleton, **64**(4), pp. 248–257.

[8] Brownstein, A. J., Ziganshin, B. A., Kuivaniemi, H., Body, S. C., Bale, A. E., and Elefteriades, J. A., 2017, "Genes Associated With Thoracic Aortic Aneurysm and Dissection: An Update and Clinical Implications," Aorta (Stanford), **5**(1), pp. 11–20.

[9] Gillis, E., Laer, L. V., and Loeys, B. L., 2013, "Genetics of Thoracic Aortic Aneurysm: At the Crossroad of Transforming Growth Factor-β Signaling and Vascular Smooth Muscle Cell Contractility," Circ. Res., **113**(3), pp. 327–340.

[10] Guo, D.-C., Pannu, H., Tran-Fadulu, V., Papke, C. L., Yu, R. K., Avidan, N., Bourgeois, S., Estrera, A. L., Safi, H. J., Sparks, E., Amor, D., Ades, L., McConnell, V., Willoughby, C. E., Abuelo, D., Willing, M., Lewis, R. A., Kim, D. H., Scherer, S., Tung, P. P., Ahn, C., Buja, L. M., Raman, C. S., Shete, S. S., and Milewicz, D. M., 2007, "Mutations in Smooth Muscle Alpha-Actin (ACTA2) Lead to Thoracic Aortic Aneurysms and Dissections," Nat. Genet, **39**(12), pp. 1488–1493.

[11] Kuang, S.-Q., Kwartler, C. S., Byanova, K. L., Pham, J., Gong, L., Prakash, S. K., Huang, J., Kamm, K. E., Stull, J. T., Sweeney, H. L., and Milewicz, D. M., 2012, "Rare, Non-Synonymous Variant in the Smooth Muscle-Specific Isoform of Myosin Heavy Chain, MYH11, R247C, Alters Force Generation in the Aorta and Phenotype of Smooth Muscle Cells," Circ. Res., **110**(11), pp. 1411–1422.

[12] Regalado, E. S., Guo, D.-C., Prakash, S., Bensend, T. A., Flynn, K., Estrera, A., Safi, H., Liang, D., Hyland, J., Child, A., Arno, G., Boileau, C., Jondeau, G., Braverman, A., Moran, R., Morisaki, T., Morisaki, H., Pyeritz, R., Coselli, J., LeMaire, S., and Milewicz, D. M., 2015, "Aortic Disease Presentation and Outcome Associated With ACTA2 MutationsCLINICAL PERSPECTIVE," Circulation: Cardiovasc. Genet., **8**(3), pp. 457–464.

[13] Schildmeyer, L. A., Braun, R., Taffet, G., Debiasi, M., Burns, A. E., Bradley, A., and Schwartz, R. J., 2000, "Impaired Vascular Contractility and Blood Pressure Homeostasis in the Smooth Muscle Alpha-Actin Null Mouse," FASEB J., **14**(14), pp. 2213–2220.

[14] Milewicz, D. M., Trybus, K. M., Guo, D.-C., Sweeney, H. L., Regalado, E., Kamm, K., and Stull, J. T., 2017, "Altered Smooth Muscle Cell Force Generation as a Driver of Thoracic Aortic Aneurysms and Dissections," Aeterioscler., Thromb., Vasc. Biol., **37**(1), pp. 26–34.

[15] Papke, C. L., Yamashiro, Y., and Yanagisawa, H., 2015, "MMP17/MT4-MMP and Thoracic Aortic Aneurysms: OPNing New Potential for Effective Treatment," Circ. Res., **117**(2), pp. 109–112.

[16] Choudhury, N., Bouchot, O., Rouleau, L., Tremblay, D., Cartier, R., Butany, J., Mongrain, R., and Leask, R. L., 2009, "Local Mechanical and Structural Properties of Healthy and Diseased Human Ascending Aorta Tissue," Cardiovasc. Pathol., **18**(2), pp. 83–91.

[17] Pasta, S., Rinaudo, A., Luca, A., Pilato, M., Scardulla, C., Gleason, T. G., and Vorp, D. A., 2013, "Difference in Hemodynamic and Wall Stress of Ascending Thoracic Aortic Aneurysms With Bicuspid and Tricuspid Aortic Valve," J Biomech., **46**(10), pp. 1729–1738.

[18] Isselbacher, E. M., 2005, "Thoracic and Abdominal Aortic Aneurysms," Circulation, **111**(6), pp. 816–828.

[19] Humphrey, J. D., Schwartz, M. A., Tellides, G., and Milewicz, D. M., 2015, "Role of Mechanotransduction in Vascular Biology: Focus on Thoracic Aortic Aneurysms and Dissections," Circ. Res., **116**(8), pp. 1448–1461.

[20] Li, C., and Xu, Q., 2007, "Mechanical Stress-Initiated Signal Transduction in Vascular Smooth Muscle Cells In Vitro and in Vivo," Cell. Signal., **19**(5), pp. 881–891.

[21] Riches, K., Clark, E., Helliwell, R. J., Angelini, T. G., Hemmings, K. E., Bailey, M. A., Bridge, K. I., Scott, D. J. A., and Porter, K. E., 2018, "Progressive Development of Aberrant Smooth Muscle Cell Phenotype in Abdominal Aortic Aneurysm Disease," J. Vasc. Res, **55**(1), pp. 35–46.

[22] Owens, G. K., Kumar, M. S., and Wamhoff, B. R., 2004, "Molecular Regulation of Vascular Smooth Muscle Cell Differentiation in Development and Disease," Physiol. Rev., **84**(3), pp. 767–801.

[23] Cox, T. R., and Erler, J. T., 2011, "Remodeling and Homeostasis of the Extracellular Matrix: Implications for Fibrotic Diseases and Cancer," Dis. Model. Mech., **4**(2), pp. 165–178.

[24] Hayashi, K., Kamiya, A., and Ono, K., 2012, *Biomechanics: Functional Adaption and Remodeling*, Springer Science & Business Media, Tokyo, Japan.

[25] Hong, Z., Sun, Z., Li, M., Li, Z., Bunyak, F., Ersoy, I., Trzeciakowski, J. P., Staiculescu, M. C., Jin, M., Martinez-Lemus, L., Hill, M. A., Palaniappan, K., and Meininger, G. A., 2014, "Vasoactive Agonists Exert Dynamic and Coordinated Effects on Vascular Smooth Muscle Cell Elasticity, Cytoskeletal Remodelling and Adhesion," J Physiol, **592**(6), pp. 1249–1266.

[26] Lacolley, P., Regnault, V., Nicoletti, A., Li, Z., and Michel, J.-B., 2012, "The Vascular Smooth Muscle Cell in Arterial Pathology: A Cell That Can Take on Multiple Roles," Cardiovasc. Res, **95**(2), pp. 194–204.

[27] Petit, C., Karkhaneh Yousefi, A.-A., Ben Moussa, O., Michel, J.-B., Guignandon, A., and Avril, S., 2021, "Regulation of SMC Traction Forces in Human Aortic Thoracic Aneurysms," Biomech. Model. Mechanobiol., **20**(2), pp. 717–731.

[28] Arribas, S. M., Hinek, A., and González, M. C., 2006, "Elastic Fibres and Vascular Structure in Hypertension," Pharmacol. Ther., **111**(3), pp. 771–791.

[29] Tsamis, A., Krawiec, J. T., and Vorp, D. A., 2013, "Elastin and Collagen Fibre Microstructure of the Human Aorta in Ageing and Disease: A Review," J. R. Soc. Interface, **10**(83), p. 20121004.

[30] Rubbia, L., and Gabbiani, G., 1989, "Phénotype Des Cellules Musculaires Lisses Artérielles et Athérosclérose," Méd./Sci., **5**(6), p. 389.

[31] Tremblay, D., Cartier, R., Mongrain, R., and Leask, R. L., 2010, "Regional Dependency of the Vascular Smooth Muscle Cell Contribution to the Mechanical Properties of the Pig Ascending Aortic Tissue," J. Biomech., **43**(12), pp. 2448–2451.

[32] Hayashi, K., and Naiki, T., 2009, "Adaptation and Remodeling of Vascular Wall; Biomechanical Response to Hypertension," J. Mech. Behav. Biomed. Mater., **2**(1), pp. 3–19.

[33] Somlyo, A. P., and Somlyo, A. V., 1994, "Signal Transduction and Regulation in Smooth Muscle," Nature, **372**(6503), pp. 231–236.

[34] Goffin, J. M., Pittet, P., Csucs, G., Lussi, J. W., Meister, J.-J., and Hinz, B., 2006, "Focal Adhesion Size Controls Tension-Dependent Recruitment of α-Smooth Muscle Actin to Stress Fibers," J. Cell. Biol., **172**(2), pp. 259–268.

[35] Wanjare, M., Kuo, F., and Gerecht, S., 2013, "Derivation and Maturation of Synthetic and Contractile Vascular Smooth Muscle Cells From Human Pluripotent Stem Cells," Cardiovasc. Res., **97**(2), pp. 321–330.

[36] Stadler, E., Campbell, J. H., and Campbell, G. R., 1989, "Do Cultured Vascular Smooth Muscle Cells Resemble Those of the Artery Wall? If Not, Why Not?," J. Cardiovasc. Pharmacol., **14**(Suppl 6), pp. S1–S8.

[37] Karnik, S. K., Brooke, B. S., Bayes-Genis, A., Sorensen, L., Wythe, J. D., Schwartz, R. S., Keating, M. T., and Li, D. Y., 2003, "A Critical Role for Elastin Signaling in Vascular Morphogenesis and Disease," Development, **130**(2), pp. 411–423.

[38] Mironov, V., 2014, *Fundamentals of Scanning Probe Microscopy*, Nizhniy Novgorod, Russia.

[39] Hegner, M., and Guntherodt, H.-J., 2001, "Nanometer Scale Science and Technology—The Impact of STM and AFM," ENFI, **144**, pp. 11–31.

[40] Whited, A. M., and Park, P. S.-H., 2014, "Atomic Force Microscopy: A Multifaceted Tool to Study Membrane Proteins and Their Interactions With Ligands," Biochim. Biophys. Acta (BBA) Biomembr., **1838**(1), pp. 56–68.

[41] Hamon, L., Curmi, P. A., and Pastré, D., 2010, "High-Resolution Imaging of Microtubules and Cytoskeleton Structures by Atomic Force Microscopy," Methods Cell Biol., **95**, pp. 157–174.

[42] Vahabi, S., Nazemi Salman, B., and Javanmard, A., 2013, "Atomic Force Microscopy Application in Biological Research: A Review Study," Iran J. Med. Sci., **38**(2), pp. 76–83.

[43] Thomas, G., Burnham, N. A., Camesano, T. A., and Wen, Q., 2013, "Measuring the Mechanical Properties of Living Cells Using Atomic Force Microscopy," J. Vis. Exp., (76), Article No. 50497.

[44] Gavara, N., 2017, "A Beginner's Guide to Atomic Force Microscopy Probing for Cell Mechanics," Microsc. Res. Technol., **80**(1), pp. 75–84.

[45] Müller, D. J., and Dufrêne, Y. F., 2011, "Atomic Force Microscopy: A Nanoscopic Window on the Cell Surface," Trends Cell Biol., **21**(8), pp. 461–469.

[46] Calzado-Martín, A., Encinar, M., Tamayo, J., Calleja, M., and San Paulo, A., 2016, "Effect of Actin Organization on the Stiffness of Living Breast Cancer Cells Revealed by Peak-Force Modulation Atomic Force Microscopy," ACS Nano, **10**(3), pp. 3365–3374.

[47] Sirghi, L., 2010, "Atomic Force Microscopy Indentation of Living Cells," Science, Technology, Applications and Education, A. Mendez-Vilas and J. Diaz, eds., Formatex, Badajoz, Spain, Vol. 1, p. 8.

[48] Rigato, A., Rico, F., Eghiaian, F., Piel, M., and Scheuring, S., 2015, "Atomic Force Microscopy Mechanical Mapping of Micropatterned Cells Shows Adhesion Geometry-Dependent Mechanical Response on Local and Global Scales," ACS Nano, **9**(6), pp. 5846–5856.

[49] Cartagena-Rivera, A. X., Wang, W.-H., Geahlen, R. L., and Raman, A., 2015, "Fast, Multi-Frequency, and Quantitative Nanomechanical Mapping of Live Cells Using the Atomic Force Microscope," Sci. Rep., **5**(1), p. 11692.

[50] Zhu, Y., He, L., Qu, J., and Zhou, Y., 2018, "Regulation of Vascular Smooth Muscle Cell Stiffness and Adhesion by [Ca2+]i: An Atomic Force Microscopy-Based Study," Microsc. Microanal., **24**(6), pp. 708–712.

[51] Pittenger, B., Erina, N., and Su, C., 2014, "Mechanical Property Mapping at the Nanoscale Using PeakForce QNM Scanning Probe Technique," *Nanomechanical Analysis of High Performance Materials*, A. Tiwari, ed., Springer Netherlands, Dordrecht, pp. 31–51.

[52] JPK Instruments AG, 2019, "Application Note: QI Mode—Quantitative Imaging with the NanoWizard 3 AFM," JPK Instruments AG, Berlin, Germany, accessed Feb. 28, 2019, https://www.jpk.com/app-technotes-img/AFM/pdf/jpk-tech-quantitative-imaging.14-1.pdf

[53] Petit, C., 2019, "Characterization of Micro/Nano-Rheology Properties of Soft and Biological Matter Combined With a Virtual Reality Haptic Exploration," Presented at the MARSS 2019 (International Conference on Manipulation Automation and Robotics at Small Scales), Helsinki, Finland, July 1–5, pp. 1–6, accessed June 12, 2019, https://hal.archives-ouvertes.fr/hal-02141911

[54] Roduit, C., Longo, G., Benmessaoud, I., Volterra, A., Saha, B., Dietler, G., and Kasas, S., May 2012, "Stiffness Tomography Exploration of Living and Fixed Macrophages," J. Mol. Recognit., **25**(5), pp. 241–246.

[55] Sehgel, N. L., Zhu, Y., Sun, Z., Trzeciakowski, J. P., Hong, Z., Hunter, W. C., Vatner, D. E., Meininger, G. A., and Vatner, S. F., 2013, "Increased Vascular Smooth Muscle Cell Stiffness: A Novel Mechanism for Aortic Stiffness in Hypertension," Am. J. Physiol. Heart Circ. Physiol., **305**(9), pp. H1281–H1287.

[56] Qiu, H., Zhu, Y., Sun, Z., Trzeciakowski, J. P., Gansner, M., Depre, C., Resuello, R. R. G., Natividad, F. F., Hunter, W. C., Genin, G. M., Elson, E. L., Vatner, D. E., Meininger, G. A., and Vatner, S. F., 2010, "Vascular Smooth Muscle Cell Stiffness as a Mechanism for Increased Aortic Stiffness With Aging," Circ. Res., **107**(5), pp. 615–619.

[57] Sehgel, N. L., Vatner, S. F., and Meininger, G. A., 2015, "Smooth Muscle Cell Stiffness Syndrome'—Revisiting the Structural Basis of Arterial Stiffness," Front. Physiol., **6**, Article No. 335.

[58] Hong, Z., Reeves, K. J., Sun, Z., Li, Z., Brown, N. J., and Meininger, G. A., 2015, "Vascular Smooth Muscle Cell Stiffness and Adhesion to Collagen I Modified by Vasoactive Agonists," PLoS One, **10**(3), p. e0119533.

[59] Lindeman, J. H. N., Ashcroft, B. A., Beenakker, J.-W. M., van Es, M., Koekkoek, N. B. R., Prins, F. A., Tielemans, J. F., Abdul-Hussien, H., Bank, R. A., and Oosterkamp, T. H., 2010, "Distinct Defects in Collagen Microarchitecture Underlie Vessel-Wall Failure in Advanced Abdominal Aneurysms and Aneurysms in Marfan Syndrome," Proc. Natl. Acad. Sci., **107**(2), pp. 862–865.

[60] Owens, G. K., Rabinovitch, P. S., and Schwartz, S. M., 1981, "Smooth Muscle Cell Hypertrophy Versus Hyperplasia in Hypertension," Proc. Natl. Acad. Sci. U. S. A., **78**(12), pp. 7759–7763.

[61] Jaminon, A., Reesink, K., Kroon, A., and Schurgers, L., 2019, "The Role of Vascular Smooth Muscle Cells in Arterial Remodeling: Focus on Calcification-Related Processes," Int. J. Mol. Sci., **20**(22), p. 5694.

[62] Li, G., Wang, M., Caulk, A. W., Cilfone, N. A., Gujja, S., Qin, L., Chen, P.-Y., Chen, Z., Yousef, S., Jiao, Y., He, C., Jiang, B., Korneva, A., Bersi, M. R., Wang, G., Liu, X., Mehta, S., Geirsson, A., Gulcher, J. R., Chittenden, T. W., Simons, M., Humphrey, J. D., and Tellides, G., 2020, "Chronic mTOR Activation Induces a Degradative Smooth Muscle Cell Phenotype," J. Clin. Invest., **130**(3), pp. 1233–1251.

[63] Hayashi, K., and Iwata, M., 2015, "Stiffness of Cancer Cells Measured With an AFM Indentation Method," J. Mech. Behav. Biomed. Mater., **49**, pp. 105–111.

[64] Poon, B., Rittel, D., and Ravichandran, G., 2008, "An Analysis of Nanoindentation in Linearly Elastic Solids," Int. J. Solids Struct., **45**(24), pp. 6018–6033.

[65] Lin, D. C., Dimitriadis, E. K., and Horkay, F., 2007, "Robust Strategies for Automated AFM Force Curve Analysis–I. Non-Adhesive Indentation of Soft, Inhomogeneous Materials," ASME J. Biomech. Eng., **129**(3), pp. 430–440.

[66] Petit, C., Guignandon, A., and Avril, S., 2019, "Traction Force Measurements of Human Aortic Smooth Muscle Cells Reveal a Motor-Clutch Behavior," Mol. Cell Biomech., **16**(2), pp. 87–108.

[67] Braunsmann, C., Seifert, J., Rheinlaender, J., and Schäffer, T. E., 2014, "High-Speed Force Mapping on Living Cells With a Small Cantilever Atomic Force Microscope," Rev. Sci. Instrum., **85**(7), p. 073703.

[68] Morkvėnaitė-Vilkončienė, I., Ramanavičienė, A., and Ramanavičius, A., 2013, "Atomic Force Microscopy as a Tool for the Investigation of Living Cells," Medicina (Kaunas), **49**(4), pp. 25–164.

[69] Caporizzo, M. A., Roco, C. M., Ferrer, M. C. C., Grady, M. E., Parrish, E., Eckmann, D. M., and Composto, R. J., 2015, "Strain-Rate Dependence of Elastic Modulus Reveals Silver Nanoparticle Induced Cytotoxicity," Nanobiomedicine, **2**, p. 9.

[70] Nawaz, S., Sánchez, P., Bodensiek, K., Li, S., Simons, M., and Schaap, I. A. T., 2012, "Cell Visco-Elasticity Measured With AFM and Optical Trapping at Sub-Micrometer Deformations," PLos One, **7**(9), pp. e45297.

[71] Win, Z., Buksa, J. M., Steucke, K. E., Gant Luxton, G. W., Barocas, V. H., and Alford, P. W., 2017, "Cellular Microbiaxial Stretching to Measure a Single-Cell Strain Energy Density Function," ASME J. Biomech. Eng., **139**(7), p. 071006.

[72] Lacolley, P., Regnault, V., and Avolio, A. P., 2018, "Smooth Muscle Cell and Arterial Aging: Basic and Clinical Aspects," Cardiovasc. Res., **114**(4), pp. 513–528.

[73] Marrese, M., Guarino, V., and Ambrosio, L., 2017, "Atomic Force Microscopy: A Powerful Tool to Address Scaffold Design in Tissue Engineering," J. Funct. Biomater., **8**(1), p. 7.

[74] Hengsberger, S., Kulik, A., and Zysset, P., 2001, "A Combined Atomic Force Microscopy and Nanoindentation Technique to Investigate the Elastic Properties of Bone Structural Units," Eur. Cell Mater., **1**, pp. 12–17.

[75] Canovic, E. P., 2016, "Characterizing Multiscale Mechanical Properties of Brain Tissue Using Atomic Force Microscopy, Impact Indentation, and Rheometry," J. Vis. Exp., (115), Article No. 54201.

[76] Lee, J.-., Rao, J., Galatioto, S., Ramirez, J. F., and Costa, K., 2015, "AFM Indentation of Aorta and Lung Reveals Tissue-Specific Micromechanical Degradation With Age in a Mouse Model of Severe Marfan Syndrome," 41st Annual Northeast Biomedical Engineering Conference (NEBEC), Troy, NY, Apr. 17–19.

[77] Hayenga, H. N., Trache, A., Trzeciakowski, J., and Humphrey, J. D., 2011, "Regional Atherosclerotic Plaque Properties in ApoE–/–Mice Quantified by Atomic Force, Immunofluorescence, and Light Microscopy," JVR, **48**(6), pp. 495–504.

[78] Oie, T., Murayama, Y., Fukuda, T., Nagai, C., Omata, S., Kanda, K., Yaku, H., and Nakayama, Y., 2009, "Local Elasticity Imaging of Vascular Tissues Using a Tactile Mapping System," J. Artif. Organs, **12**(1), pp. 40–46.

[79] Chai, C.-K., Akyildiz, A. C., Speelman, L., Gijsen, F. J. H., Oomens, C. W. J., van Sambeek, M. R. H. M., Lugt, A. V. D., and Baaijens, F. P. T., 2015, "Local Anisotropic Mechanical Properties of Human Carotid Atherosclerotic Plaques—Characterisation by Micro-Indentation and Inverse Finite Element Analysis," J. Mech. Behav. Biomed. Mater., **43**, pp. 59–68.

[80] Tracqui, P., Broisat, A., Toczek, J., Mesnier, N., Ohayon, J., and Riou, L., 2011, "Mapping Elasticity Moduli of Atherosclerotic Plaque in Situ Via Atomic Force Microscopy," J. Struct. Biol., **174**(1), pp. 115–123.

[81] Smolyakov, G., Formosa-Dague, C., Severac, C., Duval, R. E., and Dague, E., 2016, "High Speed Indentation Measures by FV, QI and QNM Introduce a New Understanding of Bionanomechanical Experiments," Micron, **85**, pp. 8–14.

[82] Gerthoffer, W. T., 2005, "Actin Cytoskeletal Dynamics in Smooth Muscle Contraction," Can J. Physiol. Pharmacol., **83**(10), pp. 851–856.

[83] Gunst, S. J., and Fredberg, J. J., 2003, "The First Three Minutes: Smooth Muscle Contraction, Cytoskeletal Events, and Soft Glasses," J. Appl. Physiol., **95**(1), pp. 413–425.

[84] Sazonova, O. V., Isenberg, B. C., Herrmann, J., Lee, K. L., Purwada, A., Valentine, A. D., Buczek-Thomas, J. A., Wong, J. Y., and Nugent, M. A., 2015, "Extracellular Matrix Presentation Modulates Vascular Smooth Muscle Cell Mechanotransduction," Matrix Biol., **41**, pp. 36–43.

[85] Clark, J. M., and Glagov, S., 1985, "Transmural Organization of the Arterial Media. The Lamellar Unit Revisited," Aeteriosclerosis, **5**(1), pp. 19–34.

[86] Davis, E. C., 1993, "Smooth Muscle Cell to Elastic Lamina Connections in Developing Mouse Aorta. Role in Aortic Medial Organization," Lab. Invest., **68**(1), pp. 89–99.